



Stack, M.M. and Abdelrahman, M.S. and Jana, B. (2010) A CFD model of erosion-corrosion of Fe at elevated temperatures in aqueous environments. *Advances in Science and Technology* (72). pp. 75-86. ISSN 1662-0356

<http://strathprints.strath.ac.uk/20221/>

Strathprints is designed to allow users to access the research output of the University of Strathclyde. Copyright © and Moral Rights for the papers on this site are retained by the individual authors and/or other copyright owners. You may not engage in further distribution of the material for any profitmaking activities or any commercial gain. You may freely distribute both the url (<http://strathprints.strath.ac.uk>) and the content of this paper for research or study, educational, or not-for-profit purposes without prior permission or charge. You may freely distribute the url (<http://strathprints.strath.ac.uk>) of the Strathprints website.

Any correspondence concerning this service should be sent to The Strathprints Administrator: eprints@cis.strath.ac.uk

A CFD model of erosion-corrosion of Fe at elevated temperatures in aqueous environments

M.M. Stack, S.M. Abdelrahman and B.D. Jana

Department of Mechanical Engineering
University of Strathclyde
James Weir Building
75 Montrose St
Glasgow
G1 1XJ, UK

Key words: CFD models, erosion-corrosion, maps

Abstract

In studies of erosion-corrosion at materials at elevated temperatures, there have been many attempts to model the process. Such models have comprised quasi-static and simulation models. However in many environments, erosion-corrosion occurs in aqueous conditions and can be considerably affected by flowing gases in dry conditions. In such cases, any accurate models of erosion-corrosion must include an algorithm due to flow in addition to the mechanics and chemistry of the tribo-corrosion interactions. In this paper, a CFD model is generated of the tribo-chemical interaction at elevated temperatures. The initial work has concentrated on modeling temperature effects in wet conditions; however, the potential application of the model to dry conditions is also outlined. The results are discussed in relation to existing erosion-corrosion models in the literature at elevated temperatures.

Introduction

Erosion-corrosion by solid particles has been the subject of much interest in the past decades due to the fact that this is a technologically challenging issue in many environments, ranging from room to elevated temperatures, and in aqueous to dry conditions [1-4]. Various diverse environments such as oil and gas drilling, advanced power generation processes and dental environments suffer from erosion interacting with corrosion. In such cases, the degradation is a function of properties of the particles, the target and the environment. Models have been constructed of the degradation based on the many variables affecting the wastage rate. [5-9]

In recent years, a relatively new development has been to construct mechanistic maps charting the transitions between the regimes [10-14]. The various criteria between the regime transitions and the variables incorporated on the maps have varied widely. Yet these maps are powerful tools for separating the tribological action from the corrosion process and their interactions. They also have the capability to identify regimes of safe and unsafe operating conditions, in addition to providing a basis for materials selection and process optimization as a function of the conditions.

In developing realistic models of erosion-corrosion, it is very important to understand the limitations of existing modelling approaches. In any process, the tribo-chemical parameters will interact with flow conditions dictated by the properties of the gas or liquid in which the particles are entrained. Yet until recently, such important effects have rarely been incorporated into erosion-corrosion models.

In this paper, a CFD model has been developed to model the effect of temperature on the erosion-corrosion in a three dimensional space. The results have been used to map temperature effects on the erosion-corrosion of a 3-D component. The potential of the model to apply to erosion-corrosion in dry conditions is discussed in this paper.

Methodology

The metal surface mechanical properties are affected by the temperature rise. Sheldon et al. [15] related the yield strength with the Vickers hardness number by the following empirical relation:

$$H_s(T) = 2.7 \sigma_y(T) \quad (1)$$

Nho [16] listed the effect of elevated temperature on the hardness of various carbon and stainless steel alloys. Das et al. [17] used the data in Shida et al. [18] to propose polynomial relationships for various materials to accurately relate the yield strength and the material temperature. A correlation relation for the carbon steel is given, based in these data as follows [17]:

$$Y(T) = 9.81(2 \times 10^{-5} T^2 - 0.0353 T + 30.871) \quad (2)$$

Thus, the target material hardness can be related to the operating temperature as:

$$H_s(T) = 26.487(2 \times 10^{-5} T^2 - 0.0353 T + 30.871) \quad (3)$$

The specific heat of the target material is also influenced by the temperature rise. From the available standard data for Fe [19], the following polynomial function can be created to represent this change:

$$C_p(T) = 17.905(2.038 \times 10^{-12} T^5 - 4.66 \times 10^{-9} T^4 + 4.22 \times 10^{-6} T^3 - 1.87 \times 10^{-3} T^2 + 0.432 T - 16.77) \quad (4)$$

Therefore, we can use equations 3 and 4, to account for the temperature effect of the target material on its mechanical properties in the erosion-corrosion modelling.

Erosion models for 3D map construction. In modelling the erosion rates at any impact angle, the second erosion model of Sundararajan [20] was found to be suitable for this new method, but also needs some adaption to account for the effect of temperature rise on the surface of the material used. The model can predict the erosion rates at different impact angles and for different particle shape. It is split into two expressions; one is for the normal impact, and the other is for the oblique impact, and is summarised here as follows; for erosion by deformation [20]:

$$Er_{def} = \frac{5.5 \times 10^{-2}}{(T_m - 436)^{0.75}} \frac{2^{n_c} \bar{f}_t V^2 \sin^2 \alpha (1 - e^2)}{n_c C_p} \quad (5)$$

for erosion by cutting:

$$Er_{cut} = \frac{5.5 \times 10^{-2} (n_c + 1) \left(\frac{\mu}{\mu_f} \right) \left(2 - \frac{\mu}{\mu_f} \right) V^2 \cos^2 \alpha}{(T_m - 436)^{0.75} (1 + \lambda) 2^{2-n_c} n_c C_p} \quad (6)$$

where:

$$\mu_f = \frac{1}{(1 + \lambda)(1 + e) \tan \alpha} \quad (7)$$

The normal and tangential coefficient of restitution can be related to the impact angle through the semi-empirical relation [21]:

$$e_n = 0.988 - 0.78 \alpha + 0.19 \alpha^2 - 0.024 \alpha^3 + 0.027 \alpha^4 \quad (8)$$

and:

$$e_t = 1.0 - 0.78 \alpha + 0.84 \alpha^2 - 0.21 \alpha^3 + 0.028 \alpha^4 - 0.022 \alpha^5 \quad (9)$$

It can also be related to the target material properties as [13]:

$$e_n = \frac{1.36 H_s^{0.625}}{E_e^{0.5} \rho_p^{0.125} V^{0.25}} \quad (9)$$

where the elastic modulus of collision (or reduced modulus of elasticity) (E_e) can be given by [22]:

$$E_e = \frac{E_t E_p}{\left[E_p (1 - \nu_t^2) + E_t (1 - \nu_p^2) \right]} \quad (10)$$

Eraslan and coworkers [23, 24] have used experimental data of Noda [25] to model the dependency of the mechanical properties of steel on temperature. They used a nonlinear fitting formulae for the experimental data and assumed constant Poisson ratio in a temperature range from 273 – 673[K]. This assumption was found to hold for most of the engineering materials such as steels. The modulus of elasticity is given as a function of temperature from [23, 24] as:

$$E = E_o \left[1 + \frac{(T - 273.16)}{T_1 \ln(T/T_2)} \right] \quad (11)$$

where $E_o = 200$ [GPa], $T_1 = 2000$ [°C] and $T_2 = 1100$ [°C].

The effect of the fluid temperature rise can be estimated by its influence in the fluid viscosity and density. A curve fitting was used to fit the available data [26] for the density and viscosity change to account for their variation with the temperature rise in [K]. For the density of water:

$$\rho_l(T) = 1.65 \times 10^{-5} T^3 - 0.02 T^2 + 7.01 T + 207.51 \quad (12)$$

and for the water viscosity variation with temperature:

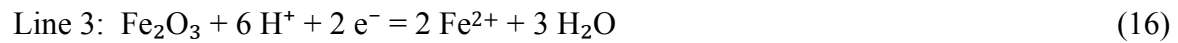
$$\mu_l(T) = 2.4 \times 10^{-5} \left[10^{\frac{247.8}{T-140}} \right] \quad (13)$$

Equations (12, 13) were used in the CFD simulation to calculate the water density at the temperature range given.

Corrosion models

Active corrosion models. Corrosion in steel is governed by several factors but mainly by the applied conditions of the solution alkalinity measured by pH scale and applied potential within the chemical reaction [27]. These are the factors that determine the corrosion process if it is in the dissolution or the passivation region, according to E-pH diagram for the Fe. Thus, to investigate the effect of the temperature rise on the corrosion rates, it is necessary to study the temperature rise effects on the E-pH diagram of the Fe.

Figure 1(a-d) shows the simplified E-pH diagrams for Fe at various temperatures ranging from 298 to 363 [K] respectively, showing how dissolution and passivation regions change with the temperature rise. The main electrochemical reactions equations involved are represented by the boundary lines numbered in Figure 1(a), and are listed as follows [27]:



In order to construct the 2D erosion-corrosion maps correctly, these lines must be represented mathematically as a function of the applied potential and pH variables. This can be done by computing the thermodynamics that govern each electrochemical reaction. The equation of every line at the given temperature levels is listed in table 1. These lines represent the transition between dissolution, passivation and immunity regions.

The corrosion rate is mainly characterised by the summation between the pure corrosion rates (K_{co}), which can be neglected because it is assumed to be very low; and the contribution of erosion to the corrosion process denoted by (ΔK_c) (also known as erosion enhanced corrosion) in the passive region. Corrosion rates in the dissolution region can be estimated by neglecting (ΔK_c) (because these are assumed to be low) and calculating the net current density [$A\ cm^{-2}$] from the Butler-Volmer equation which is dependent on the temperature. Equation 19 can be thus given as:

$$i_{met} = i_o \left[\exp\left(\frac{\beta z_m Fr (E_{ap} - E_o)}{R_o T}\right) - \exp\left(\frac{-(1-\beta) z_m Fr (E_{ap} - E_o)}{R_o T}\right) \right] \quad (19)$$

The dissolution rate can be expressed by Faraday law:

$$K_c = K_{co} = \frac{RAM\ i_{met}}{z_m\ Fr} \quad (20)$$

The Butler-Volmer equation is used in modelling the dissolution corrosion rate in both 2D and 3D erosion-corrosion maps.

Repassivation models for 3D maps. The passivation model developed in [14] is used to estimate the additive effect (ΔK_c). It should be noted that the effect of temperature is only apparent in the reduction of the target material hardness. The erosion rate is given as:

$$\Delta K_c = \pi \bar{k} \bar{h} \rho_f d_p^2 \left[\frac{\rho_p (1-e^2)}{6H_s} \right]^{0.5} (V \sin \alpha_1) \quad (21)$$

The unit given for the erosion model by equation 21 is [$kg\ impact^{-1}$]. To convert to [$kg\ m^{-2}\ s^{-1}$], equation 21 is multiplied by the particle impact flux as outlined in [13]. This can be varied according to the erosion-corrosion process being modelled. For example, if the flow is homogeneous (constant particle concentration), particle impact frequency may be given as [28]:

$$I_p = \frac{c_p V_p \sin \alpha}{m_p} \quad (22)$$

Converting to [$kg\ m^{-2}\ s^{-1}$] using equation 22; the passive layer erosion model will be [14]:

$$\Delta K_c = \frac{\pi}{m_p} c_p \bar{k} \bar{h} \rho_f d_p^2 \left[\frac{\rho_p (1-e^2)}{6H_s} \right]^{0.5} (V_p \sin \alpha_1)^2 \quad (23)$$

The constant (k) is defined as the mass ratio between the metal and its oxide created during the corrosion reaction multiplied by the number of moles of metal involved in the reaction, and is related to (k_2) in [13]; by definition as: ($k = k_2/2$).

Erosion-corrosion mapping

The total wear can be estimated as the summation of the erosion and corrosion rates and is given by:

$$K_t = K_c + K_e \quad (24)$$

where

$$K_e = K_{eo} + \Delta K_e \quad (25)$$

and

$$K_c = K_{co} + \Delta K_c \quad (26)$$

In the active regions, the erosion enhanced corrosion ΔK_c and corrosion enhanced erosion ΔK_e are neglected while in passive regions, the pure corrosion is much lower than the erosion enhanced corrosion. hence, in the active regions, the total wear is given by:

$$K_t = K_{eo} + K_{co} \quad (27)$$

and in passive regions the total wear may be given as:

$$K_t = K_{eo} + \Delta K_c \quad (28)$$

The regime boundaries needed for constructing the regime maps on the interior surfaces of the pipe are defined by the ratio K_c/K_e . and are useful in determining the transition regimes at a given applied pH and applied potential.

$$\frac{K_c}{K_e} < 0.1 \quad (\text{Erosion dominated}) \quad (29)$$

$$0.1 \leq \frac{K_c}{K_e} < 1 \quad (\text{Erosion-Corrosion dominated}) \quad (30)$$

$$1 \leq \frac{K_c}{K_e} < 10 \quad (\text{Corrosion-Erosion dominated}) \quad (31)$$

$$\frac{K_c}{K_e} \geq 10 \quad (\text{Corrosion- dominated}) \quad (32)$$

The transition boundaries for the wastage maps:

$$K_t < 1 \text{ [mm year}^{-1}\text{]} \quad (\text{low wastage}) \quad (33)$$

$$1 \leq K_t < 10 \text{ [mm year}^{-1}\text{]} \quad (\text{medium wastage}) \quad (34)$$

$$K_t \geq 10 \text{ [mm year}^{-1}\text{]} \quad (\text{high wastage}) \quad (35)$$

Slurry flow models

A dilute slurry flow of water-alumina sand particles with assumed uniform size of 10^{-3} [m] and volume fraction of 0.1 is ingested through a pipe bend inlet with bore diameter D equal to 0.078[m] and (R_c/D) ratio of 1.2. All CFD simulations were made by FLUENT ver.6.3 [29], which uses a finite volume method to solve the flow governing equations. Table 2 summarises the equations and operating and boundary conditions used in this study while Table 3 lists the mechanical and physical properties for the slurry and target material. A structured grid is performed in the near walls; for the bulk flow region, an unstructured grid was used. The imbalance between the mass flow rates in the exit boundary and the inlet one was computed to ensure mass continuity and found to be 1.144×10^{-5} [kg s⁻¹]. To validate the CFD analysis, an erosion rate comparison with the case study [30, 31] was performed, Figure 2. The validation simulation was made for SS304L stainless steel alloy using the Forder erosion model [21] as in [30]. The results in the present study were simulated for mild steel using Sundararajan's second model [20].

Results

Fig. 2 indicates the various predictions of the erosion models and it can be seen that there are similarities between the erosion rates calculated and evaluated in earlier work [30] when the values in the earlier study were used and hence this was a useful calibration exercise. The predictions on real surfaces are indicated in Fig. 3 where the highest erosion rates were observed at the bend in the pipe. Analysis of the impact frequency; Fig. 4 and the impact velocity profile. Fig. 5 indicates the area around the bend experienced the highest impact frequency and velocities.

Figures 6 and 7 show the regime maps for Fe at constant applied potentials and various pH values. For the erosion-corrosion regime maps at pH 5 and applied potential $V = -0.6$ [V] (SCE), Fig. 6, the dissolution regimes prevailed. At the pipe bend, in regions of higher particle concentration and velocity, there were transitions to erosion-dissolution and erosion-dominated regimes, Figure 6(a), and these tended to increase as the temperature increased; Figure 6(b-d). This is consistent with the Pourbaix diagrams in these conditions.

In contrast with the results at pH=5, Figure 7(a-d) shows the erosion-corrosion regimes at pH=9 and applied potential $V = -0.6$ [V] (SCE). Here, the erosion-passivation regime predominated. In these conditions, the corrosion rate decreased on the maps compared to erosion.

Discussion

The Pourbaix diagrams indicate, Fig. 1, the decrease in passivation potential as a function of increasing temperature, indicating that the aqueous corrosion regime may change significantly with temperature. This has a significance for the erosion-corrosion model as changes from dissolution to passivation controlled behavior become more likely as temperature is increased. If local changes in temperature occur over the component, such transitions may also be achieved.

The variation of erosion rates along the surface of the component, Fig. 3, indicates higher erosion rates at the elbow. This is consistent with a higher impact frequency and velocity in this location, Figs. 4-5. The maximum effects of erosion and thus the interactions with corrosion are most likely to occur in these conditions.

The regime maps, Fig. 6 at pH 5, indicate a reduction in dissolution as temperature is increased on the component, pushing the regimes into those dominated by erosion. At 363 K, erosion-dominated

behavior is the main degradation mechanism, Fig. 5(d). By contrast at pH 9, Fig. 7, erosion-passivation dominates the component, with a marginally decreased reduction in passivation affected behavior at the highest temperature, 363K. This indicates that temperature effects on the erosion-corrosion behavior at various pH values can differ markedly according to the thermodynamic stability of the corrosion product at the various temperatures.

Hence, the above demonstrates a new technique for modelling erosion-corrosion interactions in 3-dimensions. The approach enables erosion-corrosion regimes to be mapped in 3-dimensions. Further work will be to apply the analysis to other corrosion conditions, such as dry oxidizing environments.

Summary

A model has been developed for the effect of temperature on the erosion-corrosion by solid particles in aqueous conditions. Using this approach, various erosion-corrosion regimes have been mapped in 3-dimensions. The model indicates that the erosion-corrosion regimes may change significantly with increases in temperature. Further work on this model will be to apply it to other high temperature conditions, such as dry oxidizing environments.

References

- [1] M. M., Stack, S., Lekatos, and F. H., Stott, "Erosion-corrosion regimes: Number, nomenclature and justification?," *Tribology International*, 28(7), (1995), 445-451.
- [2] F. H., Stott, M. P., Jordan, S., Lekatos, M. M., Stack, and G. C., Wood, "The erosion-corrosion of alloys under oxidizing-sulfidizing conditions at high-temperature," *Wear*, 186(1), (1995), 291-298.
- [3] M. M., Stack, and Bray, L., "Interpretation of wastage mechanisms of materials exposed to elevated-temperature erosion-corrosion using erosion-corrosion maps and computer-graphics," *Wear*, 186(1), (1995), 273-283.
- [4] M. M. Stack, F. H. Stott, G. C. Wood, "Review of mechanisms of erosion-corrosion of alloys at elevated temperature, *Wear* 162, (1993), 706–712.
- [5] H. C. Meng, K. C. Ludema, "Wear models and predictive equations: their form and content," *Wear* 181-183 (Part 2), (1995), 443–457.
- [6] R. W. Lyczkowski, J. X. Bouillard, "State-of-the-art review of erosion modeling in fluid/solids systems," *Progress in Energy and Combustion Science*, 28 (6), (2002), 543–602.
- [7] H. Argeso, A. N. Eraslan, "On the use of temperature-dependent physical properties in thermomechanical calculations for solid and hollow cylinders," *International Journal of Thermal Sciences* 47, (2008), 136–146.
- [8] D. J. O'Flynn, M. S. Bingley, M. S. A. Bradley, A. J. Burnett, "A model to predict the solid particle erosion rate of metals and its assessment using heat-treated steels," *Wear* 248 (1-2), (2001), 162 – 177.
- [9] C., Davis, and P., Frawley, "Modelling of erosion-corrosion in practical geometries," *Corrosion Science*, 51(4), (2009), 769-775.

- [10] M. M., Stack, and F. H., Stott, "An approach to modeling erosion-corrosion of alloys using erosion-corrosion maps", *Corrosion Science*, 35, (1993), 1027-1034.
- [11] M. M., Stack, N., Corlett, and S., Zhou, "Construction of erosion-corrosion maps for erosion in aqueous slurries," *Materials Science and Technology*, 12, (1996), 662-672.
- [12] M. M., Stack, N., Corlett, and S., Turgoose, "Some recent advances in the development of theoretical approaches for the construction of erosion-corrosion maps in aqueous conditions," *Wear*, 233, (1999), 535-541.
- [13] M. M., Stack, B. D., Jana, "Modelling particulate erosion-corrosion in aqueous slurries: some views on the construction of erosion-corrosion maps for a range of pure metals," *Wear*, 256 (9-10), (2004), 986–1004.
- [14] M. M., Stack, S. M., Abdelrahman, B. D., Jana, "A new methodology for modelling erosion-corrosion regimes on real surfaces: Gliding down the galvanic series for a range of metal-corrosion systems," *Wear*, 268 (3-4), (2010), 533 – 542.
- [15] G. L. Sheldon, A., Kanhere, "Investigation of impingement erosion using single particle," *Wear*, 21 (1), (1972), 195–209.
- [16] K. M. Nho, "Experimental investigation of heat flow rate and directional effect on contact conductance of anisotropic ground/lapped interfaces," Ph.D. thesis, University of Waterloo, Canada, (1990).
- [17] S. K. Das, K. M., Godiwalla, S., Shubha, S. P., Mehrotra, P. K., Dey, "A mathematical model to characterize effect of silica content in the boiler fly ash on erosion behaviour of boiler grade steel," *Journal of Materials Processing Technology*, 204 (1-3), (2008), 239–247.
- [18] Y. Shida, H., Fujikawa, "Particle erosion behavior of boiler tube materials at elevated temperature," *Wear*, 103 (4), (1985), 281–296.
- [19] D. R. Lide (Ed.), "*CRC Handbook of Chemistry and Physics*," 87th Edition, Taylor and Francis, Boca Raton, FL, USA, (2007), Ch. Properties of Solids, Ch.12, p. 195, CD-ROM Version.
- [20] G. Sundararajan, "A comprehensive model for the solid particle erosion of ductile materials," *Wear*, 149 (1-2), (1991), 111 – 127.
- [21] A. Forder, M., Thew, D., Harrison, "A numerical investigation of solid particle erosion experienced within oilfield control valves," *Wear*, 216 (2), (1998), 184–193.
- [22] M. M., Stack, N., Corlett, and S., Zhou, "Some thoughts on the effect of elastic rebounds on the boundaries of the aqueous erosion-corrosion map," *Wear*, 214 (2), (1998), 175–185.
- [23] Y., Orcan, A. N., Eraslan, "Thermal stresses in elastic-plastic tubes with temperature-dependent mechanical and thermal properties," *Journal of Thermal Stresses*, 24 (11), (2001), 1097–1113.
- [24] A. N. Eraslan, Y., Orcan, "Computation of transient thermal stresses in elastic-plastic tubes: Effect of coupling and temperature-dependent physical properties," *Journal of Thermal Stresses*, 25 (6), (2002), 559-572.

- [25] N. Noda, "Thermal stresses in materials with temperature dependent properties," In: Proceedings of the NATO Advanced Research Workshop on Thermal Shock and Thermal Fatigue Behaviour of Advanced Ceramics, Kluwer Academic, MA, USA, (1993), pp. 15–26.
- [26] D. R. Lide, (Ed.), "*CRC Handbook of Chemistry and Physics*," 87th Edition, Taylor and Francis, Boca Raton, FL, USA, (2007), Ch. Fluid Properties, Ch.6, p. 2, CD-ROM Version.
- [27] M. Pourbaix, "*Atlas of Electrochemical Equilibria in Aqueous Solutions*," Pergamon Press, Oxford, New York, (1966).
- [28] B. T. Lu, J. L., Luo, F., Mohammadi, K., Wang, X. M., Wan, "Correlation between repassivation kinetics and corrosion rate over a passive surface in flowing slurry," *Electrochimica Acta*, 53 (23), (2008), 7022–7031.
- [29] FLUENT, Inc., FLUENT user's guide, Version 6.3 (2006).
- [30] R. J. K. Wood, T. F., Jones, "Investigations of sand-water induced erosive wear of AISI 3041 stainless steel pipes by pilot-scale and laboratory-scale testing," *Wear*, 255 (1), (2003), 206–218.
- [31] R. J. K. Wood, T. F., Jones, J., Ganeshalingam, N. J., Miles, "Comparison of predicted and experimental erosion estimates in slurry ducts," *Wear*, 256 (9-10), (2004), 937–947.

List of Tables:

: equations of boundary lines between the passive and dissolution regions see

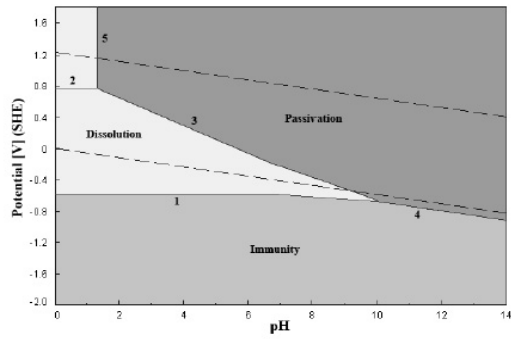
Line	Temperature [K]	Equation
Line 1	298	E= -0.618
	323	E= -0.617
	343	E= -0.618
	363	E= -0.620
Line 2	298	E= 0.771
	323	E= 0.814
	343	E= 0.848
	363	E= 0.879
Line 3	298	E= 1.076 - 0.177 pH
	323	E= 1.097 - 0.192 pH
	343	E= 1.119 - 0.204 pH
	363	E= 1.144 - 0.216 pH
Line 4	298	E= -0.054 - 0.059 pH
	323	E= -0.046 - 0.064 pH
	343	E= -0.039 - 0.068 pH
	363	E= -0.032 - 0.072 pH
Line 5	298	pH = 1.72
	323	pH = 1.47
	343	pH = 1.33
	363	pH = 1.23

Table 2: CFD modelling equations, operating and boundary conditions

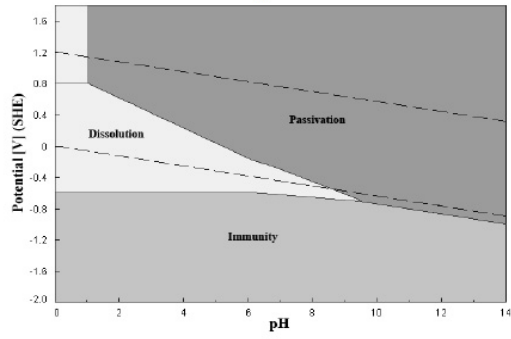
Model parameter	Water	Alumina sand
Solver equations	Navier-Stokes	DPM
Turbulence model	Standard $k - \epsilon$	
Wall treatment	Standard wall functions	
Coupling		two-way coupling
operating conditions	ambient	
inlet velocity [m s^{-1}]	3	3

Table 3: Physical and mechanical properties for the slurry and target material

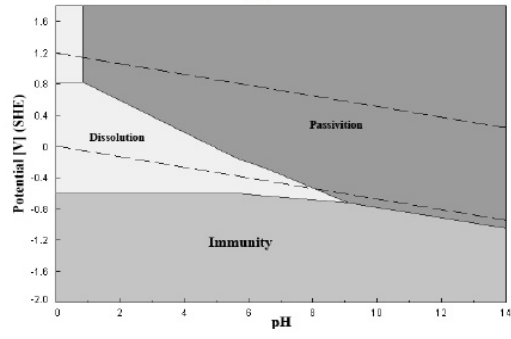
	Fluid (water)	Sand (alumina)	Target (mild steel)
density [kg m^{-3}]	998	2670	7850
particle size [m]		10^{-3}	
mass flow rate [kg s^{-1}]	14.3	3.827	



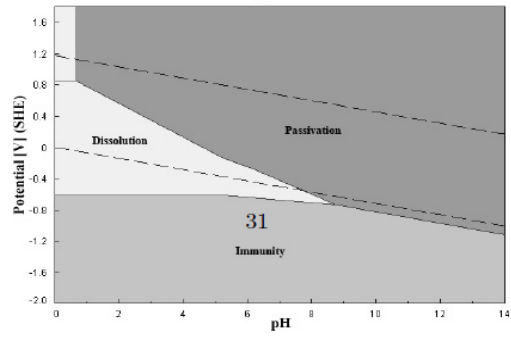
(a)



(b)



(c)



(d)

Figure 1: Simplified Pourbaix diagrams for Fe at: a) 298 b) 323 c) 343 d) 363 [K].

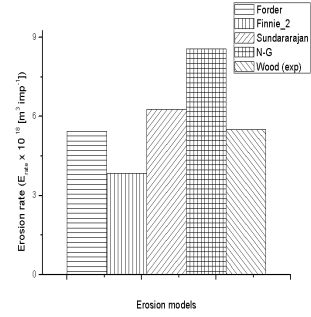


Figure 2: Prediction of erosion models and comparison with experimental results of Wood et al. [] at 298 [K].

Erosion rates [m3 imp-1]



Figure 3: Erosion rates contours on the outer surface predicted by (DPM) Discrete Particle Method at 298 [K].

Impact frequency [imp m-2 s-1]

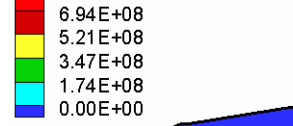


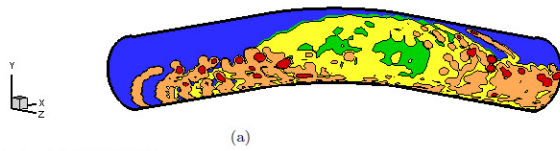
Figure 4: Impact frequency by (DPM) Discrete Particle Method at 298 [K].

Impact Velocity [m.s-1]

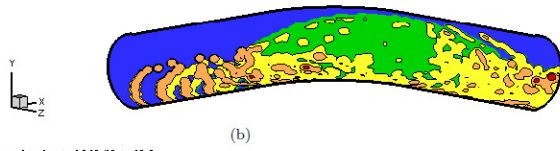


Figure 5: Impact velocity profile on the surface of the elbow-pipe at 298 [K].

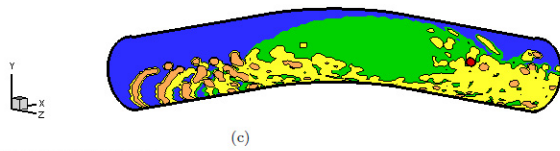
■ Dissolution dominated [$K_p/K_s \geq 10$]
 ■ Dissolution erosion [$1 \leq K_p/K_s < 10$]
 ■ Erosion dissolution [$0.1 \leq K_p/K_s < 1$]
 ■ Erosion dominated [$0 \leq K_p/K_s < 0.1$]
 ■ No erosion



■ Dissolution dominated [$K_p/K_s \geq 10$]
 ■ Dissolution erosion [$1 \leq K_p/K_s < 10$]
 ■ Erosion dissolution [$0.1 \leq K_p/K_s < 1$]
 ■ Erosion dominated [$0 \leq K_p/K_s < 0.1$]
 ■ No erosion



■ Dissolution dominated [$K_p/K_s \geq 10$]
 ■ Dissolution erosion [$1 \leq K_p/K_s < 10$]
 ■ Erosion dissolution [$0.1 \leq K_p/K_s < 1$]
 ■ Erosion dominated [$0 \leq K_p/K_s < 0.1$]
 ■ No erosion



■ Dissolution dominated [$K_p/K_s \geq 10$]
 ■ Dissolution erosion [$1 \leq K_p/K_s < 10$]
 ■ Erosion dissolution [$0.1 \leq K_p/K_s < 1$]
 ■ Erosion dominated [$0 \leq K_p/K_s < 0.1$]
 ■ No erosion

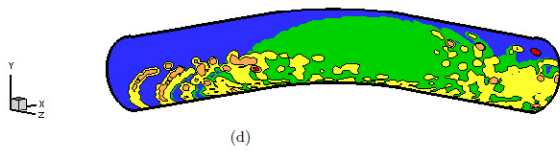
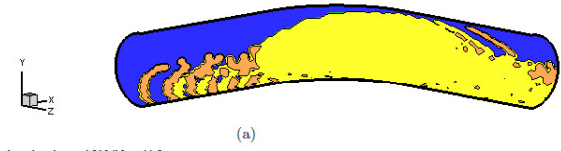
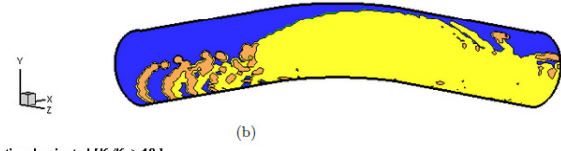


Figure 6: Regime maps for Fe at pH = 5, V = -0.6 [V](SCE) at: a) 298 b) 323 c) 343 d) 363 [K].

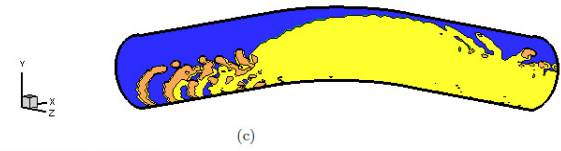
■ Passivation dominated [$K_p/K_s \geq 10$]
 ■ Passivation erosion [$1 \leq K_p/K_s < 10$]
 ■ Erosion passivation [$0.1 \leq K_p/K_s < 1$]
 ■ Erosion dominated [$0 \leq K_p/K_s < 0.1$]
 ■ No erosion



■ Passivation dominated [$K_p/K_s \geq 10$]
 ■ Passivation erosion [$1 \leq K_p/K_s < 10$]
 ■ Erosion passivation [$0.1 \leq K_p/K_s < 1$]
 ■ Erosion dominated [$0 \leq K_p/K_s < 0.1$]
 ■ No erosion



■ Passivation dominated [$K_p/K_s \geq 10$]
 ■ Passivation erosion [$1 \leq K_p/K_s < 10$]
 ■ Erosion passivation [$0.1 \leq K_p/K_s < 1$]
 ■ Erosion dominated [$0 \leq K_p/K_s < 0.1$]
 ■ No erosion



■ Passivation dominated [$K_p/K_s \geq 10$]
 ■ Passivation erosion [$1 \leq K_p/K_s < 10$]
 ■ Erosion passivation [$0.1 \leq K_p/K_s < 1$]
 ■ Erosion dominated [$0 \leq K_p/K_s < 0.1$]
 ■ No erosion

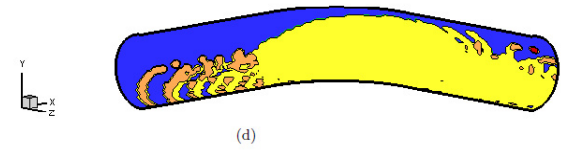


Figure 7: Regime maps for Fe at pH = 9, V = -0.6 [V](SCE) at: a) 298 b) 323 c) 343 d) 363 [K].